Full-wave simulations of ICRF and HHFW heating regimes in toroidal plasma with non-Maxwellian distribution functions

N. Bertelli[1], E. J. Valeo[1], D. L. Green[2], M. Gorelenkova[1], C. K. Phillips[1], M. Podestà[1], J. P. Lee[3], J. C. Wright[3], and E. F. Jaeger[4]

[1]Princeton Plasma Physics Laboratory, Princeton, New Jersey 08543, USA
[2]Oak Ridge National Laboratory, Post Office Box 2008, Oak Ridge, Tennessee 37831-6169, USA
[3]Plasma Science and Fusion Center, MIT, Cambridge, MA 02139, USA
[4]XCEL Engineering Inc., 1066 Commerce Park Drive, Oak Ridge, Tennessee 37830, USA

E-mail: `nbertell@pppl.gov`

Abstract. At the power levels required for significant heating and current drive in magnetically-confined toroidal plasma, modification of the particle distribution function from a Maxwellian shape is likely [T. H. Stix, *Nucl. Fusion*, 15:737 1975], with consequent changes in wave propagation and in the location and amount of absorption. In order to study these effects computationally, both the finite-Larmor-radius and the high-harmonic fast wave (HHFW), full-wave, hot-plasma toroidal simulation code, `TORIC` [M. Brambilla, *Plasma Phys. Control. Fusion* **41**, 1 (1999) and M. Brambilla, *Plasma Phys. Control. Fusion* **44**, 2423 (2002)], have been extended to allow the prescription of arbitrary velocity distributions of the form $f(v_\parallel, v_\perp, \psi, \theta)$. For hydrogen (H) minority heating of a deuterium (D) plasma with anisotropic Maxwellian H distributions, the fractional H absorption varies significantly with changes in parallel temperature but is essentially independent of perpendicular temperature. On the other hand, for HHFW regime with anisotropic Maxwellian fast ion distribution, the fractional beam ion absorption varies mainly with changes in the perpendicular temperature. The evaluation of the wave-field and power absorption, through the full wave solver, with the ion distribution function provided by either a Monte-Carlo particle and Fokker-Planck codes is also examined for Alcator C-Mod and NSTX plasmas. Non-Maxwellian effects generally tends to increase the absorption with respect to the equivalent Maxwellian distribution.

1. Introduction

The injection of waves in the ion cyclotron frequency range is a well-established method of heating and driving current in magnetically confined toroidal plasma. A straightforward estimate suggests that, at rf power levels which are sufficiently high that finite enhancements in temperature or current are achieved, the ion velocity distribution functions are expected to be significantly modified from a thermal, Maxwellian shape [1]. Since the absorption of energy and momentum are overwhelmingly through collisionless wave-particle interactions, local in velocity space, these distribution function modifications will, generally, result in finite changes in the amount and spatial location of absorption. Inclusion of these modifications, ultimately computed self-consistently together with the wave fields, is required to more faithfully model experimental results and to more accurately design future devices.

There has been substantial progress recently to address these considerations. More recently, the all-orders (in Larmor radius to wavelength) global-wave solver `AORSA` [2] has been coupled to the `CQL3D` Fokker-Planck code [3, 4]. The combination has been iteratively solved to self-consistently compute wave-fields and ion distribution functions [5]. Similar work has been done with other RF numerical tools, such as `METS` [6, 7], `GNET-TASK/WM` [8], `SSPQL/ TORIC` v.6 package [9, 10], `CYRANO` [11] `ORBIT-RF/AORSA` [12], `VENUS-LEMan` in the `SCENIC` package [13], `EVE` [14, 15], and `SELFO-light` [16].

Here, we describe the extension of both the finite Larmor radius (FLR) and the high harmonic fast wave (HHFW) versions of the `TORIC` code [17, 18] to include non-Maxwellian distribution functions. The version of `TORIC` used in this work corresponds to the `TORIC`'s version also named `TORIC` v.5 and currently implemented in the `TRANSP` code [19]. Indeed, this work is a starting point to be able to treat self-consistently in `TRANSP` the evolution of the H minority and beam ion population in the presence of RF heating. As mentioned above, there are two versions of the code: (i) FLR and (ii) HHFW regimes. The former makes use of the assumption that the ion Larmor radius $\rho_{\rm i}$ is small-but-finite compared to the scale of wave field variation perpendicular to the local magnetic field direction, $\hat{\mathbf{b}}$, *i.e.*, $\rho_{\rm i}|\hat{\mathbf{b}} \times \nabla A/A| << 1$, for any field component A. This approximation greatly reduces computational burden while still accurately reproducing results obtained from the more general codes when the small-Larmor-radius approximation is verified *a posteriori*. More specifically, `TORIC` takes into account FLR corrections only up to $\omega = 2\Omega_{\rm c,i}$ (where ω and $\Omega_{\rm c,i}$ are the angular frequency and the ion cyclotron angular frequency, respectively). On the other hand, in the HHFW version of the code, coefficients of the wave equation are replaced by the corresponding elements of the full hot-plasma dielectric tensor where the k (k is the wave-vector) value in the argument of the Bessel functions is obtained by solving the local dispersion relation for the fast wave (FW) root.

The code extensions are presented in detail in Section 2 together with a brief description of the code. The numerical implementation is presented in Section 3. Results of applications are presented in Section 4 for both a isotropic and anisotropic distribution functions in Alcator C-Mod [20] and NSTX [21] plasmas . Finally, a discussion and the main conclusions of the work are summarized in Section 5.

2. Code description

2.1. The finite-Larmor-radius full-wave `TORIC` *version*

The `TORIC` code solves the vector wave equation

$$\nabla \times \nabla \times \mathbf{E} = \frac{\omega^2}{c^2}\left[\mathbf{E} + \frac{4\pi i}{\omega}(\mathbf{J}^{\rm P} + \mathbf{J}^{\rm A})\right] \tag{1}$$

for the vector electric field $\mathbf{E}$. The undriven plasma is assumed time independent and toroidally symmetric. Therefore, the response to a prescribed antenna current density $\mathbf{J}^{\rm A}(\mathbf{x}_{\rm p}, \phi, t)$ as a function of poloidal position $\mathbf{x}_{\rm p}$, toroidal angle ϕ, and time t, can be obtained by summation of responses to each Fourier component $\mathbf{J}^{\rm A}(\mathbf{x}_{\rm p}, n_\phi, \omega)\exp[i(n_\phi\phi - \omega t)]$ with frequency ω and toroidal mode number n_ϕ. The plasma current density $\mathbf{J}^{\rm P}$,

$$\mathbf{J}^{\rm P} \equiv \sum_s q_j \int d\mathbf{v}\, \mathbf{v}\, f_s(\mathbf{x}, \mathbf{v}; \omega) \tag{2}$$

requires the solution for the particle distribution functions $f_s(\mathbf{x}, \mathbf{v}; \omega)$, for each species s, which is computed by solving the linearized Vlasov equation with several assumptions: the particle gyro-radii are small compared to the scale of field variation perpendicular to the local magnetic field direction, $\mathbf{b} \equiv \mathbf{B}/|\mathbf{B}|$; the effects of drifts across the magnetic flux surfaces are negligible; multiple resonant wave-particle interactions are uncorrelated. The small-Larmor-radius approximation reduces the response to cross-field variations of $\mathbf{E}$ from an integral to a differential form. Spatial dependence is further decomposed into variation within and across poloidal flux surfaces, $\psi(\mathbf{x}) = $ const. Fourier decomposition of variation within surfaces,

$$A(r, z) = \sum_m A_m(\psi)\, e^{im\theta} \tag{3}$$

and projection of the wave equation onto test functions $\mathbf{F}(\psi)$ with compact support transforms the system into a dense block (in m) - tridiagonal (in ψ) system which

is soluble using standard numerical methods. By virtue of this decomposition, the local parallel component of the wave-vector is explicitly represented as

$$k_\parallel(\theta,\psi) \equiv \mathbf{k}\cdot\mathbf{b} = (m\nabla\theta + n_\phi\nabla\phi)\cdot\mathbf{b} \tag{4}$$

This representation facilitates the required computation of the elements of the local susceptibility tensor χ_s relating the current in species s, $\mathbf{J}_s^{\mathrm{P}}$ to the driving electric field

$$\mathbf{J}_s^{\mathrm{P}} = -\frac{i\omega}{4\pi}\,\chi_s\cdot\mathbf{E}\,. \tag{5}$$

In the original version of `TORIC` code, the elements of the local susceptibility tensor χ_s are restricted to the Maxwellian case. However, in a local coordinate (Stix [22]) frame ($\hat{\mathbf{x}}$, $\hat{\mathbf{y}}$, $\hat{\mathbf{z}}$), with $\hat{\mathbf{z}} = \mathbf{b}$, $\mathbf{k}\cdot\hat{\mathbf{y}} = 0$, to second order in $k_\perp v_\perp/\Omega_c$ ($k_\perp$ and $v_\perp$ are the perpedicular components of the wave-vector and the velocity, respectively), and for arbitrary velocity distribution functions of the form

$$f_s(\mathbf{v}) = f_s(v_\perp, v_\parallel) \tag{6}$$

the components of χ can be written as [23]

$$\begin{aligned}
\chi_{xx} &= \frac{\omega_{\mathrm{p,s}}^2}{\omega}\left[\frac{1}{2}\left(A_{1,0}+A_{-1,0}\right) - \frac{\lambda}{2}\left(A_{1,1}+A_{-1,1}\right) + \right.\\
&+ \left.\frac{\lambda}{2}\left(A_{2,1}+A_{-2,1}\right)\right]\\
\chi_{xy} &= -\chi_{yx} = i\frac{\omega_{\mathrm{p,s}}^2}{\omega}\left[\frac{1}{2}\left(A_{1,0}-A_{-1,0}\right) + \right.\\
&- \left.\lambda\left(A_{1,1}-A_{-1,1}\right) + \frac{\lambda}{2}\left(A_{2,1}-A_{-2,1}\right)\right]\\
\chi_{xz} &= +\chi_{zx} = -\chi_{yx} = \frac{\omega_{\mathrm{p,s}}^2}{\omega}\left(\frac{1}{2}\frac{k_\perp}{\omega}\right)\left[\left(B_{1,0}+B_{-1,0}\right) + \right.\\
&- \left.\lambda\left(B_{1,1}+B_{-1,1}\right) + \frac{\lambda}{2}\left(B_{2,1}+B_{-2,1}\right)\right]\\
\chi_{yy} &= \frac{\omega_{\mathrm{p,s}}^2}{\omega}\left[2\lambda A_{0,1} + \frac{1}{2}\left(A_{1,0}+A_{-1,0}\right) + \right.\\
&- \left.\frac{3\lambda}{2}\left(A_{1,1}+A_{-1,1}\right) + \frac{\lambda}{2}\left(A_{2,1}+A_{-2,1}\right)\right]\\
\chi_{yz} &= -\chi_{zy} = i\frac{\omega_{\mathrm{p,s}}^2}{\omega}\left(\frac{k_\perp}{\omega}\right)\left[B_{0,0} - \lambda B_{0,1} + \right.\\
&- \frac{1}{2}\left(B_{1,0}+B_{-1,0}\right) - \lambda\left(B_{1,1}+B_{-1,1}\right)\\
&- \left.\frac{\lambda}{4}\left(B_{2,1}+B_{-2,1}\right)\right]\\
\chi_{zz} &= \frac{2\omega_{\mathrm{p}}^2}{k_\parallel w_\perp^2}\left[(1-\lambda)B_{0,0} + \right.\\
&+ \left.\int_{-\infty}^{+\infty}\mathrm{d}v_\parallel\int_0^{+\infty}\mathrm{d}v_\perp v_\perp\frac{v_\parallel}{\omega}f_0(v_\parallel,v_\perp)\right]\\
&+ \frac{\lambda}{2}\frac{\omega_{\mathrm{p}}^2}{\omega}\left[2\frac{\omega-\omega_{\mathrm{c}}}{k_\parallel w_\perp^2}B_{1,0} + 2\frac{\omega+\omega_{\mathrm{c}}}{k_\parallel w_\perp^2}B_{-1,0}\right]
\end{aligned} \tag{7}$$

where

$$\lambda \equiv \frac{1}{2}\left(\frac{k_\perp w_\perp}{\Omega_{\mathrm{c}}}\right)^2\,, \tag{8}$$

with

$$w_\perp^2 \equiv \int_{-\infty}^{\infty}\mathrm{d}v_\parallel\int_0^{+\infty}2\pi v_\perp\mathrm{d}v_\perp v_\perp^2 f_0(v_\parallel,v_\perp)\,. \tag{9}$$

Here, the coefficients

$$\begin{aligned}
\left\{\begin{array}{c} A_{n,j} \\ B_{n,j}\end{array}\right\} &= \int_{-\infty}^{\infty}\mathrm{d}v_\parallel\left\{\begin{array}{c} 1 \\ v_\parallel\end{array}\right\}\frac{1}{\omega - k_\parallel v_\parallel - n\Omega_{\mathrm{c}}}\times\\
&\times\int_0^{+\infty}2\pi v_\perp\mathrm{d}v_\perp H_j(v_\parallel,v_\perp)
\end{aligned} \tag{10}$$

with

$$\begin{aligned}
H_0(v_\parallel,v_\perp) &= \frac{1}{2}\frac{k_\parallel w_\perp^2}{\omega}\frac{\partial f_0}{\partial v_\parallel} - \left(1-\frac{k_\parallel v_\parallel}{\omega}\right)f_0(v_\parallel,v_\perp)\\
H_1(v_\parallel,v_\perp) &= \frac{1}{2}\frac{k_\parallel w_\perp^2}{\omega}\frac{\partial f_0}{\partial v_\parallel}\frac{v_\perp^4}{w_\perp^4} + \\
&- \left(1-\frac{k_\parallel v_\parallel}{\omega}\right)f_0(v_\parallel,v_\perp)\frac{v_\perp^2}{w_\perp^2}\,.
\end{aligned} \tag{11}$$

These equations have been implemented in the new code extension (see Section 3) in order to deal with arbitrary distribution functions and its applications are shown in Section 4.

2.2. The high-harmonic fast wave full-wave `TORIC` *version*

The HHFW version of the code makes use of the so-called "Quasi-local" approximation (see details in [18]). The 0th-order FLR coefficients of the wave equation are replaced by the corresponding elements of the full hot-plasma dielectric tensor in which the k^2 value in the argument of the Bessel functions is obtained by solving the local dispersion relation for FWs. At each point the resulting wave equation, which is still in differential form along the radial coordinate, has the same dispersion relation as the full integral wave equation, although only for FWs.

Similarly to the FLR case described above, the extensions of HHFW version consists mainly in the implementation of the full-hot susceptibility tensor χ for arbitrary velocity distribution functions instead of the original implementation which was restricted to the Maxwellian case. In particular, the elements of the local susceptibility tensor χ for arbitrary velocity distribution functions are of the form [22]

$$\begin{aligned}
\boldsymbol{\chi}_{\mathrm{s}} &= \frac{\omega_{\mathrm{ps}}^2}{\omega}\int_0^{+\infty}2\pi v_\perp\mathrm{d}v_\perp\times\\
&\times\int_{-\infty}^{+\infty}\mathrm{d}v_\parallel\hat{\mathbf{z}}\hat{\mathbf{z}}\frac{v_\parallel^2}{\omega}\left(\frac{1}{v_\parallel}\frac{\partial f}{\partial v_\parallel} - \frac{1}{v_\perp}\frac{\partial f}{\partial v_\perp}\right)_{\mathrm{s}} +
\end{aligned}$$

$$+\frac{\omega_{\rm ps}^2}{\omega}\int_0^{+\infty}2\pi v_\perp {\rm d}v_\perp \times$$
$$\times\int_{-\infty}^{+\infty}{\rm d}v_\parallel\sum_{n=-\infty}^{+\infty}\left[\frac{v_\perp U}{\omega-k_\parallel v_\parallel-n\Omega_{\rm cs}}\mathbf{T}_n\right] \quad (12)$$

where

$$U\equiv\frac{\partial f}{\partial v_\perp}+\frac{k_\parallel}{\omega}\left(v_\perp\frac{\partial f}{\partial v_\parallel}-v_\parallel\frac{\partial f}{\partial v_\perp}\right) \quad (13)$$

and

$$\mathbf{T}_n=\begin{pmatrix}\frac{n^2J_n^2(z)}{z^2} & \frac{inJ_n(z)J_n'(z)}{z} & \frac{nJ_n^2(z)v_\parallel}{zv_\perp}\\ -\frac{inJ_n(z)J_n'(z)}{z} & (J_n'(z))^2 & -\frac{iJ_n(z)J_n'(z)v_\parallel}{v_\perp}\\ \frac{nJ_n^2(z)v_\parallel}{zv_\perp} & \frac{iJ_n(z)J_n'(z)v_\parallel}{v_\perp} & \frac{J_n^2(z)v_\parallel^2}{v_\perp^2}\end{pmatrix}, \quad (14)$$

with $z\equiv\frac{k_\perp v_\perp}{\Omega_{\rm cs}}$.

3. Numerical implementation

The perpendicular velocity integrals produce smoothly varying functions of $v_\parallel$ whose product with the singular function $S=(\omega-k_\parallel v_\parallel-n\Omega)^{-1}$ must then be integrated in $v_\parallel$. For a non-drifting Maxwellian parallel-velocity distribution function with thermal velocity $v_{\rm th}$, these integrals can be represented in terms of the plasma dispersion function $Z(\zeta/v_{\rm th})$ [24] where $\zeta=(\omega-n\Omega)/k_\parallel$. For more general distributions, the integrations must be done numerically. Since these integrals are computed numerous times in forming the matrix system of field equations, efficient evaluation is essential. Further, since the co-factor of S is smooth, the resultant parallel integral's dependence on ζ will be smooth as well. We use this observation by evaluating the integrals at uniformly spaced points ζ_k and then interpolating the results to the desired value of ζ. Efficiency is gained by specifying the distribution function, and thus the co-factors, on the same, uniform, parallel velocity mesh, $v_k=k\,\Delta v$. Specifically, at a mesh point k, the integrals are of the form

$$I_k=\int dv\frac{C(v)}{v-v_k}\,. \quad (15)$$

We approximate the cofactors

$$C(v)=\sum_j c_jT_j\,, \quad (16)$$

where $c_j=C(v_j)$ and where T_j is a linear tent function surrounding v_j

$$T_j=\begin{cases}1-\frac{|v-v_j|}{\Delta v} & \text{if } |v-v_j|\le\Delta v,\\ 0 & \text{otherwise.}\end{cases} \quad (17)$$

Then

$$I_k=\sum_j\int dv\frac{f_jT_j}{v-v_k}=\sum_j f_jK_{j-k}=\sum f_{j+k}K_j. \quad (18)$$

where the kernel

$$K_j=\int_{-1}^1 dv\frac{1-|v|}{v+j\Delta v}=\begin{cases}\ln(\frac{j+1}{j-1})-j\ln(\frac{j^2}{j^2-1}) & |j|>1,\\ \pm\ln 4 & j=\pm1,\\ i\pi & j=0.\end{cases} \quad (19)$$

The convolutions incur modest computational cost.

The approach described here has been originally used for the non-Maxwellian extension of the `TORIC` code in the lower hybrid frequency regime [25]. Furthermore, such method also motivated an improvement of the algorithm reducing the complexity from $\mathcal{O}(N^2)$ (which is what we use in this work) to $\mathcal{O}(N\log N)$, with N being the dimension of the core matrix [26, 9].

4. Applications

4.1. Parameters used when distribution function is provided by an analytical functional form

To validate the algorithm, calculations are presented of both minority hydrogen heating in a plasma equilibrium constructed from Alcator C-Mod tokamak data and HHFW heating regime in a NSTX plasma equilibrium. The electron density profile as a function of the square root of the normalized poloidal flux for the Alcator C-Mod discharge is shown in Figure 1(a). The electron and ion temperature profiles are shown in Figure 1 (b). The corresponding plots for the NSTX plasma are shown in Figure 2. The toroidal field at the magnetic axis is 5 (0.53) Tesla for Alcator C-Mod (NSTX). The toroidal plasma current is 627 (868) kA for Alcator C-Mod (NSTX). The magnetic axis major radius is 68.26 (101.34) cm for Alcator C-Mod (NSTX). For Alcator C-Mod case: the plasma consists of 7% fractional number density of hydrogen and 93% deuterium. The wave parameters are: frequency $f=$ 78 MHz and toroidal wavenumber $n_\phi=10$, which places the fundamental H and second harmonic D resonances at 0.62 cm radially with respect to the magnetic axis location. The ion-ion hybrid resonance and cutoffs are at -2.9 and -1.8 cm, respectively (with respect to the magnetic axis location). For NSTX case: the plasma consists of 86.5% fractional number of density of (thermal) deuterium 8% of beam deuterium (fast ions). An effective temperature of the beam ions ($T_{\rm bi}$) given by [27]

$$T_{\rm bi}=\frac{2}{3}\frac{u}{n_{\rm bi}} \quad (20)$$

is used. In Eq. 20 u and $n_{\rm bi}$ are the total energy density profile and the density of the beams ions, respectively, evaluated by `NUBEAM` [28, 29]. The wave parameters are: frequency $f=30$ MHz and toroidal wavenumber $n_\phi=8$, which places the second and eleventh harmonic D resonances at the very edge of the high-field side and the low-field side, respectively. The choice of the n_ϕ

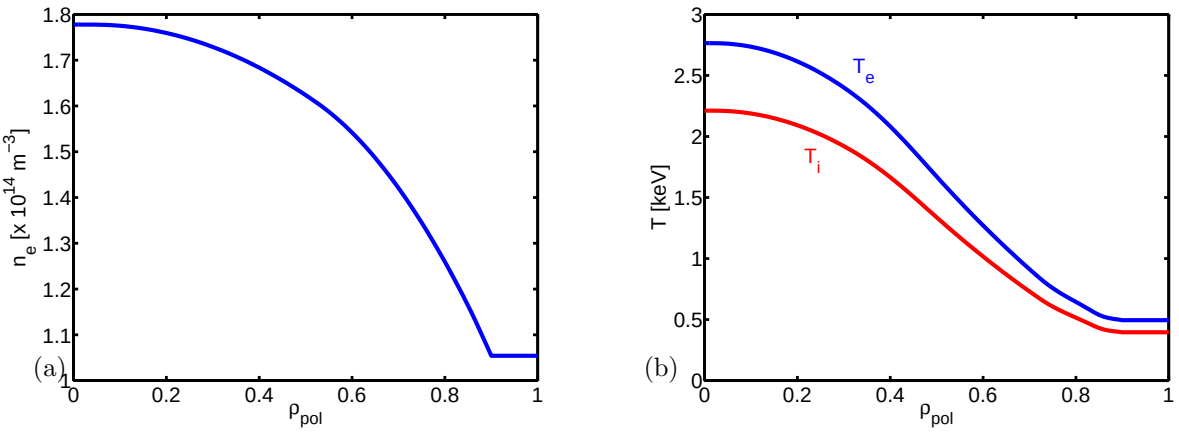

Figure 1. (a) The electron density profile, $n_{\rm e}$ as a function of the square root of the normalized poloidal flux, $\rho_{\rm pol}$ for an Alcator C-Mod plasma. (b) The electron and (common) ion temperature profiles as a function of $\rho_{\rm pol}$.

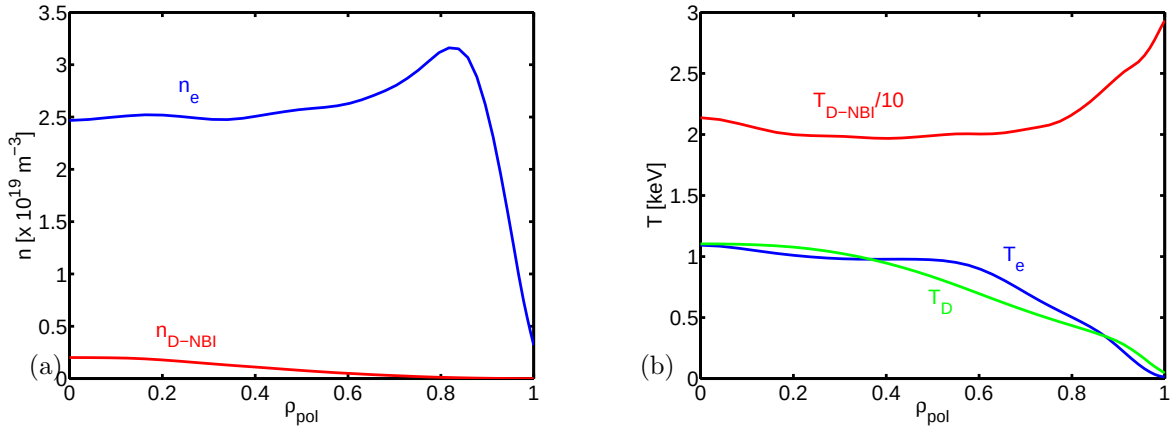

Figure 2. (a) The electron density ($n_{\rm e}$) and beam ion ($n_{\rm D-NBI}$) profiles as a function of the square root of the normalized poloidal flux ($\rho_{\rm pol}$) for a NSTX plasma. (b) The electron ($T_{\rm e}$), thermal deuterium ($T_{\rm D}$) and beam ion temperature ($T_{\rm D-NBI}$) (rescaled by a factor 10) profiles as a function of $\rho_{\rm pol}$.

value is mainly done to get a large absorption by fast ions.

4.2. Isotropic Maxwellian distributions

4.2.1. IC minority heating regime The reference calculation assumes isotropic Maxwellian distributions, using the Z function to evaluate χ. Several qualitative features are clearly visible in the surface plot of Re(E_-), where $E^- \equiv E_x - iE_y$ (in Stix coordinates) shown in 3 . The long wavelength fast wave, launched from the low-field side midplane is converted near the magnetic axis into a combination of moderate wavelength ion cyclotron waves (ICW, emanating rightward, toward the low field side) and short wavelength ion Bernstein waves (IBW, emanating leftward, toward the high field side). The relative power absorbed by second harmonic D, fundamental H and by the electrons for each wave branch is presented in Table 1 in the column labeled "Reference". To check the accuracy of the method, the results were re-computed with the minority H susceptibility calculated numerically as described in Section 3 for a Maxwellian distribution prescribed on a uniform numerical mesh of $N_{v_\parallel} = 500$ points and $N_{v_\perp} = 100$ points. The mesh range is $-c/100 \leqslant v_\parallel \leqslant c/100$ and $0 \leqslant v_\perp \leqslant c/100$ where $c = 3\times10^{10}$ cm/s is the speed of light. As shown in Table 1, the power flow channels are well converged to the reference case with differences less than $1-2\%$. A more discriminating measure of convergence is shown in Figure 4 . Figure 4 shows the real part of the three components of the wave electric field (E_-, E_+, and $E_\parallel$) on the midplane both in high (left column) and low (right column) field regions. There one can see an excellent agreement between the "Reference" (solid (black) curve) and "Numerical" (dashed (red) curve) cases.

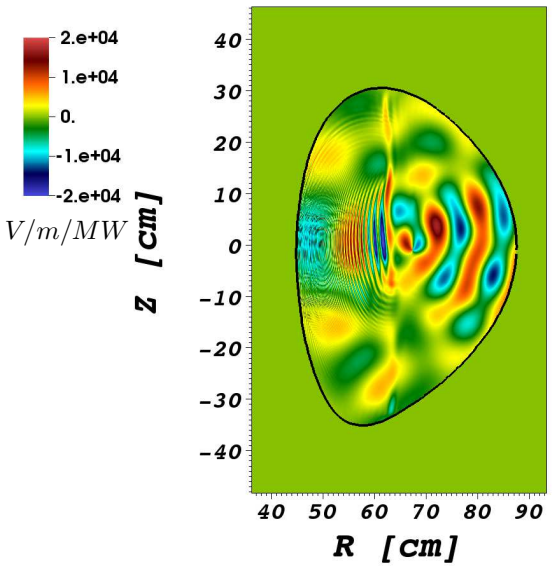

Figure 3. Real part of the right-handed wave electric field, Re(E_-), for an Alcator C-Mod plasma described in subsection 4.1.

Absorbed fraction	Reference	Numerical
2^{nd} Harmonic D	10.18	10.28
Fundamental H	69.95	68.81
Electrons - FW	11.35	11.91
Electrons - IBW	8.53	9.00

Table 1. Alcator C-Mod: Power flow to each species. The reference simulation corresponds to the original Maxwellian case while the numerical simulation numerically computed minority H susceptibility χ_H (Eqs. 7-11) assuming a Maxwellian functional form of the representation of the distribution function.

Other cases with different resolutions in $v_\parallel$ and $v_\perp$ (not shown here) have been performed always obtaining an excellent agreement between reference and numerical cases in terms of electric field propagation, power density profiles, and total absorbed power.

4.2.2. HHFW heating regime Figure 5 shows the surface plot of Re(E_-) where the long wavelength fast wave are launched from the low-field side midplane. The relative power absorbed by D, fast ions (D-NBI), and electrons is presented in Table 2 in the column labeled "Reference". As similarly done for IC minority heating regime, in order to assess the accuracy of the method, the results were re-computed with fast ions susceptibility calculated numerically as described in Section 3 for a Maxwellian distribution prescribed on a uniform numerical mesh of $N_{v_\parallel} = 100$ points, $N_{v_\perp} = 50$ points, and $N_{N_\perp^2} = 35$. The mesh range is $-c/20 \leqslant v_\parallel \leqslant c/20$, $0 \leqslant v_\perp \leqslant c/20$, and $-3 \times 10^4 \leqslant N_\perp^2 \leqslant 9.5 \times 10^4$. As shown in Table 2, the power flow channels are well converged to the reference case with differences less than 1%. Moreover, Figure 6 shows the real part of the three components of the wave electric field (E_-, E_+, and $E_\parallel$) on the midplane both in high (left column) and low (right column) field sides. There one can see an excellent agreement between the "Reference" (solid (black) curve) and "Numerical" (dashed (red) curve) cases.

Absorbed fraction	Reference	Numerical
D	0.22	0.22
D - NBI	73.88	73.58
Electrons	25.90	26.21

Table 2. NSTX: Power flow to each species. The Reference simulation corresponds to the original Maxwellian case while "Numerical" simulation uses a numerically computed susceptibility χ_{D-NBI} (Eqs. 12-14) assuming a Maxwellian functional form of the representation of the distribution function.

As done in IC minority heating regime, other cases with different resolutions in $v_\parallel$, $v_\perp$ and $N_\perp^2$ (not shown here) have been performed always obtaining an excellent agreement between reference and numerical cases in terms of electric field propagation, power density profiles, and total absorbed power. These additional tests have also shown a smooth $N_\perp^2$ dependence of the components of χ, which allow us to decrease $N_{N_\perp^2}$ mesh points significantly reducing the computational time in evaluating the full hot plasma χ tensor.

4.3. Anisotropic Maxwellian distributions (bi-Maxwellian)

4.3.1. IC minority heating regime The sensitivity of the principal absorption channel at the fundamental hydrogen resonance to changes in the shape of the hydrogen distribution was investigated by performing two series of computations, assuming an anisotropic Maxwellian form for the H distribution

$$f_H(v_\parallel, v_\perp) = (2\pi)^{-3/2}(v_{\mathrm{th},\parallel} v_{\mathrm{th},\perp}^2)^{-1} \times \\ \times \exp[-(v_\parallel/v_{\mathrm{th},\parallel})^2 - (v_\perp/v_{\mathrm{th},\perp})^2] \qquad (21)$$

with $v_{\mathrm{th},\parallel} = \sqrt{(2C_\parallel T(\psi)/m_H)}$, $v_{\mathrm{th},\perp} = \sqrt{2C_\perp T(\psi)/m_H)}$, with constants $C_\parallel$ and $C_\perp$ parameterizing the scans. The fundamental H absorption fraction, P_H varied by less than two percent when $C_\perp$ was varied from 0.5 to 5, with $C_\parallel$ held fixed at unity. In contrast the second series, in which $C_\perp$ was fixed at unity and $C_\parallel$ was varied showed a significant variation. For $C_\parallel = \{0.5, 1., 3., 5.\}$, the corresponding $P_\mathrm{H} = \{61.27, 70.50, 90.46, 94.18\}$. In addition, while the absorption profile is localized to the resonant layer for small $C_\parallel$ it is significantly broadened radially at for large $C_\parallel$. This is clearly demonstrated in Figure 7

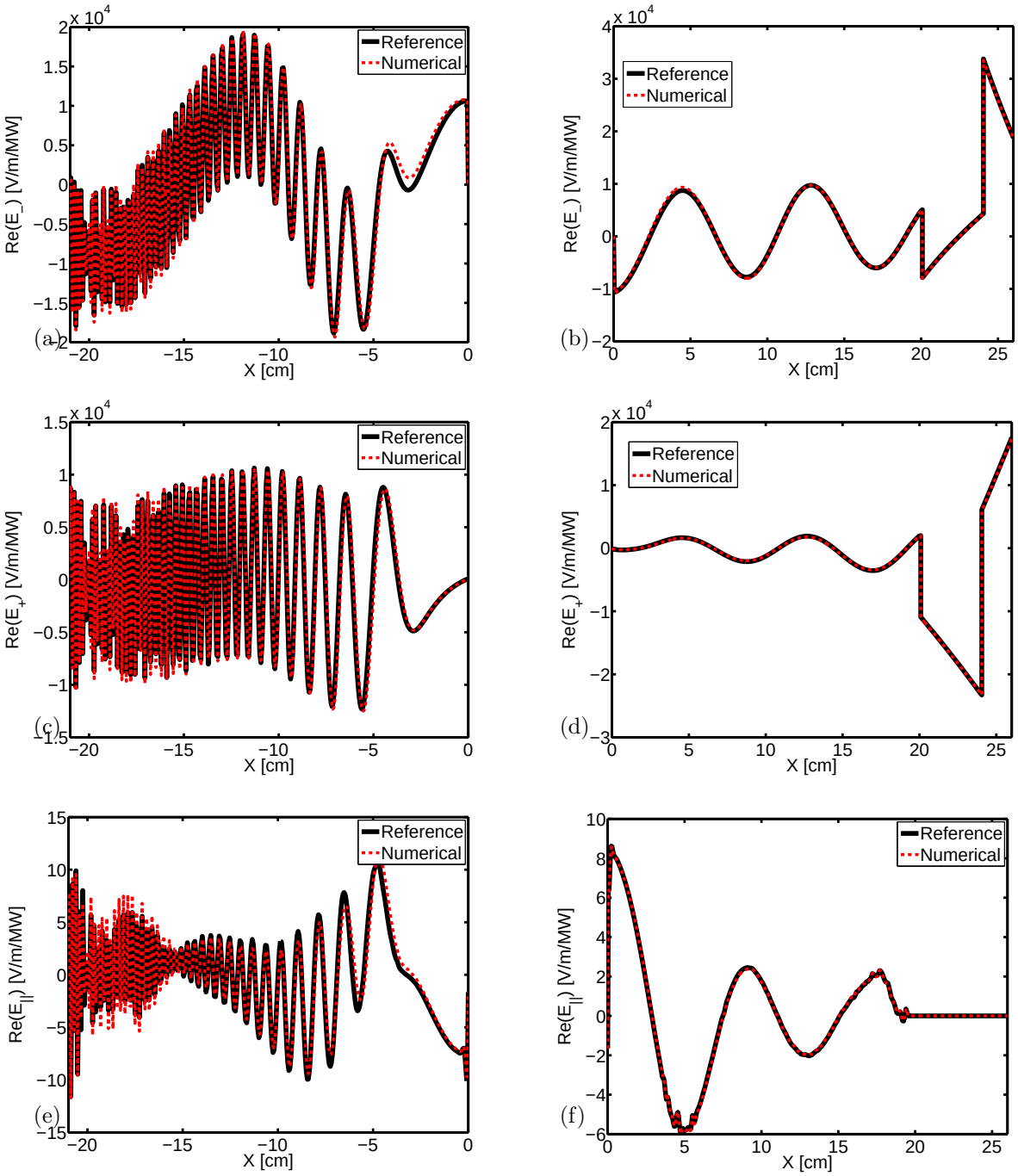

Figure 4. Figures (a) and (b): Real part of the right-handed wave electric field, Re(E_-), both in the high field side region (Fig. (a)) and in the low field line region (Fig. (b)) on the midplane for an Alcator C-Mod plasma described in subsection 4.1. The solid (black) curve represents the "Reference" case while the dashed (red) curve represents the results were re-computed with the minority H susceptibility calculated numerically. Figures (c) and (d): Real part of the left-handed wave electric field, Re(E_+), both in the high field side region (Fig. (c)) and in the low field line region (Fig. (d)). Figures (e) and (f): Real part of the parallel wave electric field, Re($E_\parallel$), both in the high field side region (Fig. (e)) and in the low field line region (Fig. (f)).

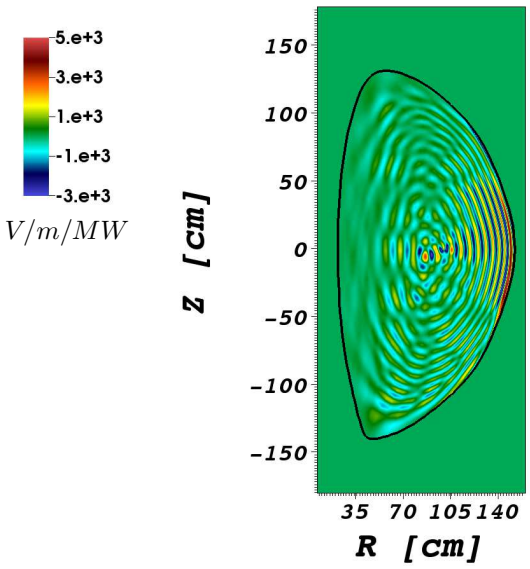

Figure 5. Real part of the right-handed wave electric field, $\mathrm{Re}(E_-)$, for a NSTX plasma described in subsection 4.1.

where the absorption vs. (R, Z) is shown for $C_\parallel = 0.5$ (Fig. 7(a)), $C_\parallel = 1.0$ (Fig. 7(b)), and $C_\parallel = 5.$ (Fig. 7(c)).

4.3.2. HHFW heating regime As similarly done above, two series of computations assuming an anisotropic Maxwellian form for the fast ions (D-NBI) population in NSTX plasma have been performed. The fast ion absorption fraction, $P_{\mathrm{D-NBI}}$, shows a significant variation when $C_\perp$ was varied from 0.5 to 5, with $C_\parallel$ held fixed at unity. In particular, for $C_\perp = \{0.5, 1., 3., 5.\}$, the corresponding $P_{\mathrm{D-NBI}} = \{70.06, 73.56, 62.84, 48.48\}$. In contrast, when $C_\perp$ was fixed at unity and $C_\parallel$ was varied, $P_{\mathrm{D-NBI}}$, varied by less than one percent. This behavior is the opposite with respect to what has been found in the IC minority heating regime. However, the absorption profile tends to be localized to the resonant layer for small $C_\parallel$ as shown in Figure 8 in agreement with the results show in the previous subsection. In this figure the absorption vs. (R,Z) is shown for $C_\parallel = 0.5$ (Fig. 8(a)) $C_\parallel = 1.0$ (Fig. 8(b)), and $C_\parallel = 5.$ (Fig. 8(c)).

For the fast ion distributions in NSTX plasma, an additional application has been performed assuming a slowing down distribution function as described in the following section.

4.4. Slowing down distributions for beam ion species in HHFW heating regime

Another functional form of the distribution function for the beam ion species which has been implemented in the generalization of TORIC v.5 is a slowing-down distribution [30]

$$f_{\mathrm{D-NBI}}(v_\parallel, v_\perp) = \begin{cases} \frac{A}{v_c^3} \frac{1}{1+(v/v_c)^3} & \text{for } v < v_{\mathrm{m}}, \\ 0 & \text{for } v > v_{\mathrm{m}} \end{cases} \qquad (22)$$

where $v_{\mathrm{m}} \equiv \sqrt{2E_{\mathrm{D-NBI}}/m_{\mathrm{D}}}$ is the maximum velocity corresponding to the injected energy $E_{\mathrm{D-NBI}}$ of the beam ions. Also, $A = 3/[4\pi \ln(1+\delta^{-3})]$ with $\delta \equiv \frac{v_c}{v_{\mathrm{m}}}$, and
$v_c^3 = 3\sqrt{\pi}(m_e/m_{\mathrm{D}})Z_{\mathrm{eff}} v_{\mathrm{th}}^3$ where $Z_{\mathrm{eff}} \equiv \sum_{\mathrm{ions}} Z_i^2 n_i/n_e$. The fast ion absorption fraction, $P_{\mathrm{D-NBI}}$, shows a significant variation when $E_{\mathrm{D-NBI}}$ was varied from 30 to 120 keV, with $Z_{\mathrm{eff}} = 2$. In particular, for $E_{\mathrm{D-NBI}} = \{30, 60, 90, 120\}$ keV, the corresponding $P_{\mathrm{D-NBI}} = \{77.84, 75.85, 70.97, 64.71\}$. This result recalls the behavior found in bi-Maxwellian case when the parameter $C_\perp$ was varied indicating that the interaction between fast ions and fast waves occurs mainly in the perpendicular direction with respect to the magnetic field [1] . However, the absorption profile tends to be localized to the resonant layer for small $E_{\mathrm{D-NBI}}$ as shown in Figure 9 in agreement with the results show in the bi-Maxwellian case for both IC minority and HHFW heating regimes (see Figures 7 and 8). In particular, figure 9 shows the power density vs. (R,Z) for $E_{\mathrm{D-NBI}} = 30$ keV (Fig. 9(a)), $E_{\mathrm{D-NBI}} = 60$ keV (Fig. 9(b)), $E_{\mathrm{D-NBI}} = 90$ keV (Fig. 9(c)),and $E_{\mathrm{D-NBI}} = 120$ keV (Fig. 9(d)).

4.5. Numerical distributions

The main goal of this extension of TORIC is to enable the code to deal with (numerical) distribution function provided by either Monte-Carlo particle or Fokker-Planck codes. In this section we describe our calculations by using (i) a distribution function obtained from the Fokker-Planck code CQL3D [3, 4] for an Alcator C-Mod plasma and (ii) a distribution function obtained from the Monte-Carlo particle code NUBEAM [28, 29] for a NSTX plasma.

4.5.1. IC minority heating regime The TORIC extension can also utilize numerical distribution functions obtained from the Fokker-Planck code CQL3D for IC minority heating regime. This is a crucial step in ultimately closing the loop between RF and Fokker-Planck solvers and the evolution of the distribution of the H minority. Indeed, this will be shown in a future paper where a RF quasi-linear diffusion operator will be implemented in the TORIC code [31].

Figure 10 shows an example of distribution function of the H minority obtained from the iteration between the full wave code AORSA and the Fokker-Planck code CQL3D for Alcator C-Mod plasma [32, 33]. More specifically, Figure 10(a) and (b) correspond to the distribution functions at 0th and 4th iteration,

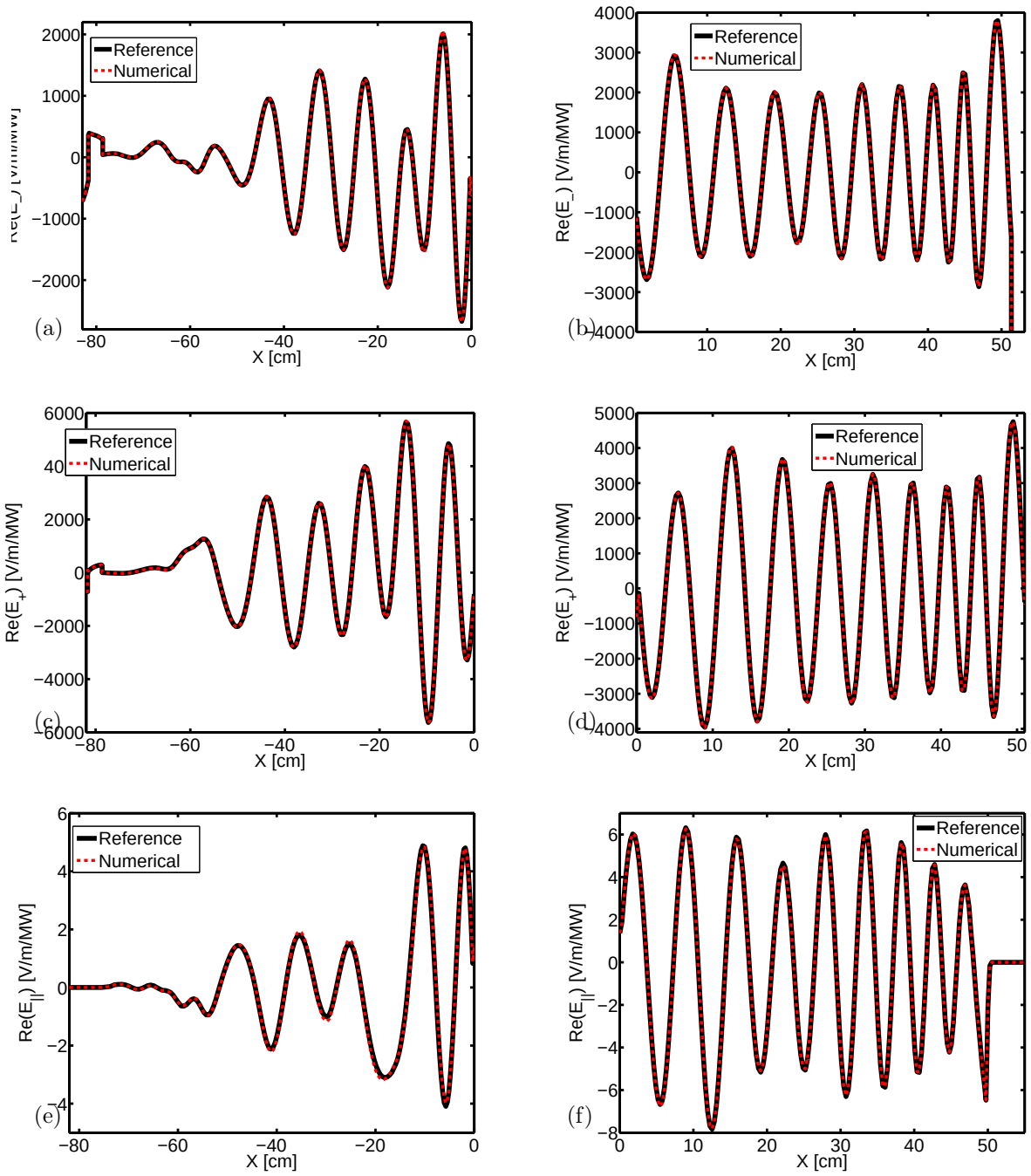

Figure 6. Figures (a) and (b): Real part of the right-handed wave electric field, Re(E_-), both in the high field side region (Fig. (a)) and in the low field line region (Fig. (b)) on the midplane for a NSTX plasma described in subsection 4.1. The solid (black) curve represents the "Reference" case while the dashed (red) curve represents the results were re-computed with the susceptibility calculated numerically. Figures (c) and (d): Real part of the left-handed wave electric field, Re(E_+), both in the high field side region (Fig. (c)) and in the low field line region (Fig. (d)). Figures (e) and (f): Real part of the parallel wave electric field, Re($E_\parallel$), both in the high field side region (Fig. (e)) and in the low field line region (Fig. (f)).

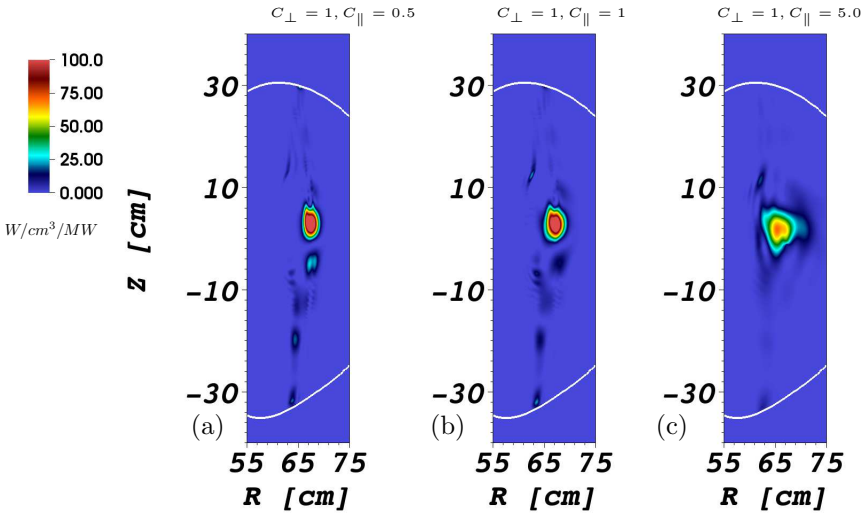

Figure 7. Contour plots of fundamental absorption by minority hydrogen (zoomed around the resonance), represented by a bi-Maxwellian distribution function (see Eq. 21) in an Alcator C-Mod plasma for $C_\perp = 1.0$ and different $C_\parallel$ values (shown in the plots). The white curve represents the last closed flux surface. Units are Watts/cm^3 at 1MW incident power.

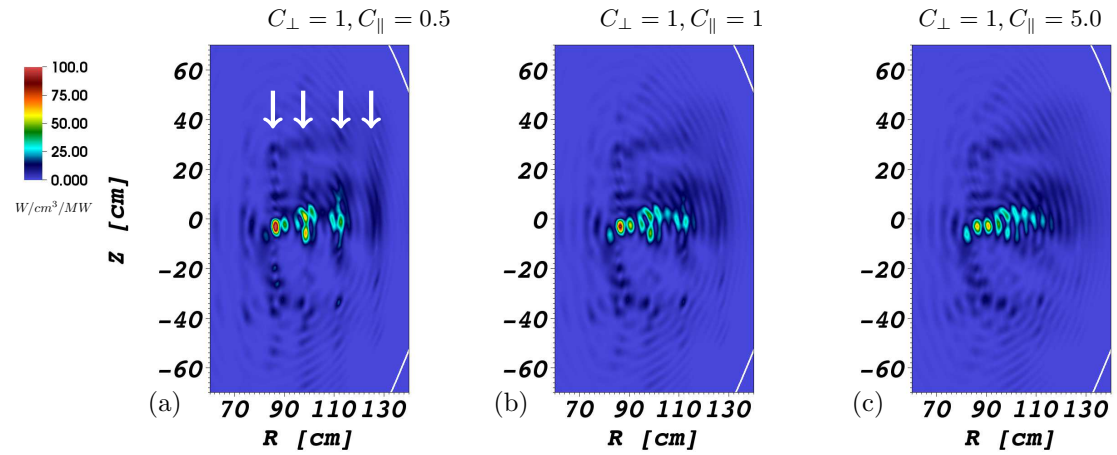

Figure 8. Contour plots of the absorption by beam ions (zoomed around the cyclotron resonances) represented by a bi-Maxwellian distribution function in a NSTX plasma for $C_\perp = 1.0$ and different $C_\parallel$ values (shown in the plots). The white curve represents the last closed flux surface. The white arrows in Figure (a) indicates the deuterium cyclotron resonance layers ($n = 7, 8, 9$, and 10). Units are Watts/cm^3 at 1MW incident power.

respectively. Both distribution functions are plotted at $\rho_{\rm pol} = 0.2$. It is important to note that at 0th iteration the distribution function is a Maxwellian distribution (we refer to as "Maxwellian case") while at the 4th iteration the RF tail is formed (see, four energy levels (10, 250, 500, and 1000 keV) for reference) (we refer to as "non-Maxwellian case"). In order to evaluate the impact of the non-Maxwellian effects in the power deposition of the H minority, we compute numerically χ for both the numerical distributions shown in Figure 10 on a uniform numerical mesh of $N_{v_\parallel} = 500$ points and $N_{v_\perp} = 200$ points. The mesh range $-c/100 \leqslant v_\parallel \leqslant c/100$ and $0 \leqslant v_\perp \leqslant c/100$. Figure 11 shows the contour plot of the power density of the H minority for both the Maxwellian case (Fig. (a)) and the non-Maxwellian case (Fig. (b)). One can note that the non-Maxwellian effects tend to broaden the power deposition profile as clearly seen in Fig. b. This result reflects what has been shown for a bi-Maxwellian by varying the parallel temperature (see Figure 7). Furthermore, Table 3 shows that the power flow to H minority increases when the RF tail at higher energy is formed with respect to the Maxwellian case.

4.5.2. HHFW heating regime Besides the capability to deal with numerical distribution functions obtained from the Fokker-Planck code `CQL3D` for IC minority heating regime, the extension of `TORIC` is also able

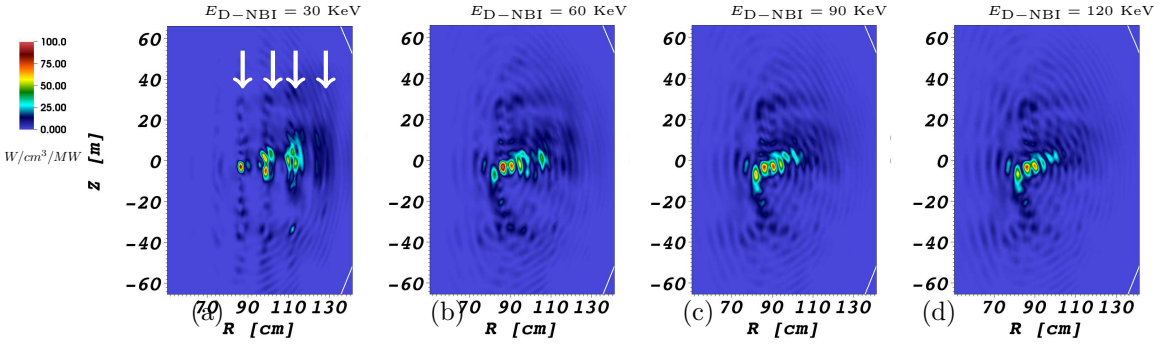

Figure 9. Contour plots of the absorption by beam ions represented by a slowing down distribution function (see Eq. 22) in a NSTX plasma for different NBI injected energy E_{D-NBI} (shown in the plots). The white curve represents the last closed flux surface. The white arrows in Figure (a) indicates the deuterium cyclotron resonance layers ($n = 7, 8, 9$, and 10).

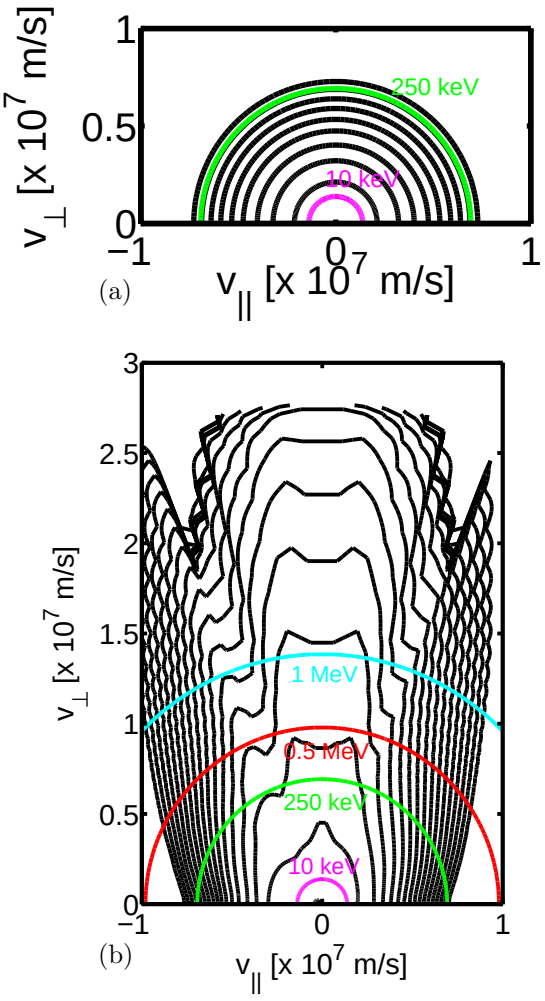

Figure 10. Minority H distribution function from the iteration between `AORSA` and `CQL3D` for Alcator C-Mod at $\rho_{pol} = 0.2$. Figures (a) and (b) show the distribution at 0th and 4th iteration respectively.

Absorbed fraction	Maxw.	non-Maxw
2nd Harmonic D	18.38	11.85
Fundamental H	58.82	72.89
Electrons - FW	12.94	9.40
Electrons - IBW	9.85	5.86

Table 3. Power flow to each species. The Maxw. case corresponds to the numerical Maxwellian distribution from `CQL3D` at step 0 while the Non-Maxw case corresponds to the numerical non-Maxwellian distribution obtained by `CQL3D` at step 4 (see Figure 10 as an example).

now to use directly the particle lists generated by the Monte-Carlo particle code `NUBEAM`. This feature is particularly important for the study of the interaction between fast waves and energetic particles, such as fast ions generated by NBI as in NSTX.

Here the coupling of a particle based code (`NUBEAM`) with a continuum code (`TORIC`) is handled by `P2F` [34, 35]. The `P2F`‡ code converts a discrete particle list to a 4-D continuum distribution function. The 4 dimensions are 2 cylindrical in space (R, z) and 2 cylindrical in velocity space ($v_\perp$, $v_\parallel$) with parallel being along the local B field direction of the corresponding spatial grid point. Conceptually `P2F` generates a histogram of the input particles in it's 4-D grid. However, since the full-wave code takes velocity space derivatives of the beam distribution function, that function must be smooth enough for the derivatives to be robust. This means that a box-function style histogram, even at 10^6 particles, produces a histogram where noise dominates the derivatives, especially at the larger velocities. To resolve this issue `P2F` implements two smoothing techniques. The first is a velocity space Gaussian particle shape with user defined width (c.f., [35] for details), and the second is to distribute each computational particle along its unperturbed guiding center bounce orbit weighted according to time spent

‡ Available at https://github.com/ORNL-Fusion/p2f.

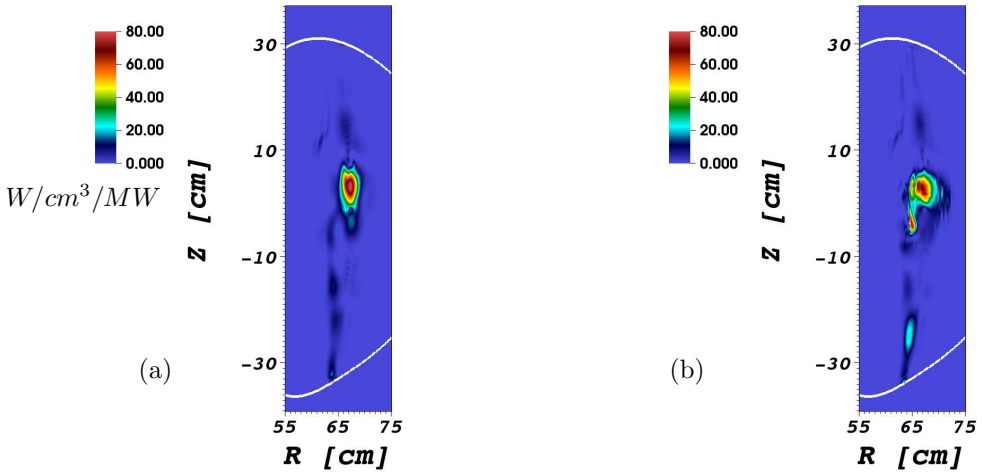

Figure 11. H minority absorption profile from the TORIC solver for: (a) CQL3D Maxwellian case (initial step); (b) CQL3D non-Maxwellian case (final step)

in each of the 4-D histogram bins. While this approach results in robust velocity space derivatives, it will not reveal velocity space gradients sharper than those defined by the Gaussian particle width, i.e., we must choose the minimum Gaussian width necessary to ensure robustness of the velocity space derivatives for a particular number of computational particles, and also choose a number of computational particles in the NUBEAM calculation to ensure insensitivity of the resulting full-wave calculation to that number.

As done in the previous sections, to test our implementation we first check the Maxwellian distribution case by making use of the P2F code. First, we have artificially generated a particle list representing a Maxwellian distribution in a NSTX plasma geometry with analytical temperature and density profiles given by analytical kinetic profiles for electron and fast ion population. More specifically, the parameters were:

$$n_e(\rho_{pol}=0) \;= 2.5\times10^{13}\mathrm{cm}^{-3} \tag{23}$$
$$n_e(\rho_{pol}=1) \;= 2.5\times10^{12}\mathrm{cm}^{-3} \tag{24}$$
$$T_e(\rho_{pol}=0) \;= 1\mathrm{keV};\; T_e(\rho_{pol}=1)=0.1\mathrm{keV} \tag{25}$$
$$n_{FI}(\rho_{pol}=0)=2.0\times10^{12}\mathrm{cm}^{-3} \tag{26}$$
$$n_{FI}(\rho_{pol}=1)=2.0\times10^{11}\mathrm{cm}^{-3}; \tag{27}$$

and for the fast ion temperatures employed are given by

$$T_{FI}(\rho_{pol})=(T_{FI,0}-T_{FI,1})\left(1-\rho_{pol}^2\right)^5+T_{FI,1} \tag{28}$$

with

$$T_{FI,0}\equiv T_{FI}(\rho_{pol}=1) \;= 20\mathrm{keV}; \tag{29}$$
$$T_{FI,1}\equiv T_{FI}(\rho_{pol}=1)=5\mathrm{keV} \tag{30}$$

Second, we have run P2F by using the Maxwellian particles list to obtain a continuum distribution function. Third, we have numerically evaluated χ and we have run TORIC. Finally, we have compared the results with the reference case. Figure 12 shows indeed the results of this comparison. In particular, in Figure 12 the black curve indicates the reference case. In addition, there are other four cases which are obtained assuming a particles list with 2×10^3 (red curve), 10^4 (green), 10^5 (magenta curve), and 10^6 (cyan curve) particles. The numerical case converges to excellent agreement with the reference case as the number of particles is increased. It is also important to note two points: (i) the total power to the fast ions among the three cases with 10^4, 10^5, and 10^6 number of particles differs by less than 1%; (ii) with 10^4 particles a good converge is already achieved. This is an important point for the future application in time dependent modeling frameworks, such as TRANSP simulations.

Finally, Figure 13 shows the fast ion distribution function at $R=1$ m and $z=0$ m obtained from the P2F code starting from a NUBEAM particles list for a NSTX shot 141711 at time = 0.47 s without HHFW. The number of particles used for this case in NUBEAM are 53115. For reference, the 90 keV beam injection energy is represented by the white curve while the half (45 keV) and third energy (30 keV) components are represented by red and magenta curves, respectively. As done for the minority heating regimes, Figure 14 shows the comparison of the equivalent Maxwellian distribution and the realistic distribution starting from NUBEAM, in terms of the 2D fast ion power density. For equivalent Maxwellian distribution we mean that we use an effective temperature of the beam ions temperature (T_{bi}) given by Eq. 20. From figure 14, one can only see a slight change (a slight broadening) in the profile when the realistic distribution is adopted.

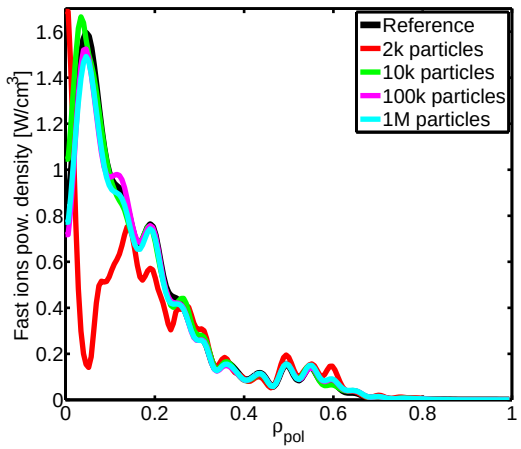

Figure 12. RF power deposition on fast ions from `TORIC` using `P2F` distributions as a function of $\rho_{\rm pol}$. Black curve represents the reference case whereas the color curves indicate different particle number adopted in the calculations as shown in the legend.

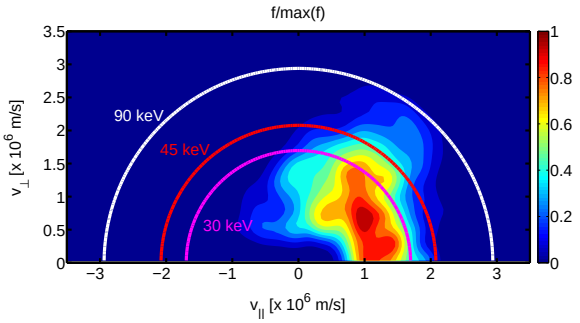

Figure 13. Fast ion distribution function at $R = 1$ m and $z = 0$ m obtained from the `P2F` code starting from a `NUBEAM` particles list for a NSTX plasma without HHFW (shot 141711 at time = 0.47 s).

Absorbed fraction	Maxw.	Non-Maxw
D	41.80	37.99
D-NBI	53.94	58.12
Electrons	4.26	3.89

Table 4. Power flow to each species. The Maxw. case corresponds to an equivalent Maxwellian temperature for the fast ions population (cf. Eq. 20) while the Non-Maxw case corresponds to the numerical non-Maxwellian distribution obtained by `P2F` starting from a `NUBEAM` particles list.

However, there is a variation in power flow to the different species, as shown in Table 4. As expected, a larger power flow to fast ions is found when a realistic distribution is considered with respect to the equivalent Maxwellian case. It is worth noting that the relatively small differences in the power flow to fast ions between equivalent Maxwellian and the realistic case shown in Table 4, are due to the fact that the distribution function in the case considered here is not affected by RF therefore the distribution function does not have a large RF tail to higher energies. In fact, as shown in the bi-Maxwellian case, for a large variation of the perpendicular temperature/energy the power flow has varied significantly. The consideration of a realistic distribution obtained starting from `NUBEAM` and affected by RF, will be part of a future work which requires the study of a quasi-linear RF diffusion operator (also called RF kick operator) in `NUBEAM`. In this scenario, we might expect a larger amount of power deposited to the fast ions population due to a larger distribution function tail formed by the RF application. This could have a strong impact in the recent NSTX experimental observations where HHFW was able to fully suppress Alfvén activities, such as Toroial Alfvén Eigenmodes (TAEs) and Global Alfvén Eigenmodes (GAEs) [36].

5. Conclusions

The ICRF wave simulation code `TORIC` has been generalized to allow prescription of arbitrary particle distribution functions of the form $f(v_\parallel, v_\perp, \theta, \psi)$ in the computation of the plasma susceptibility in both the minority and HHFW heating regimes. The algorithm was validated by recovering results for RF heating in Alcator C-MOD and NSTX obtained by computing χ using analytic approximations to the plasma dispersion function for the case when all species are Maxwellian. The application of bi-Maxwellian distribution function shows a different behavior in the total absorbed power between the most common IC minority and HHFW heating regimes. In particular, for IC minority heating regime, the total absorbed power at the H fundamental is insensitive to variations in the perpendicular temperature ($T_\perp$), but varies with changes in parallel temperature ($T_\parallel$), whereas for HHFW regime, the behavior is reversed, namely, the total absorbed power by fast ions is insensitive to variations in $T_\parallel$, thus reflecting the well-known Doppler broadening effect of parallel temperature on the absorption profile. However, for both heating regimes, the power density profiles vary with changes in $T_\parallel$. Similar results have been found and shown for HHFW heating regime assuming a slowing-down distribution function. The impact of the non-Maxwellian effects with respect to the Maxwellian case has been evaluated in both IC minority heating regime by using a distribution function obtained from a Fokker-Planck code `CQL3D` and HHFW heating regime by using a distribution function obtained from the Monte-Carlo particle code `NUBEAM`. Both cases indicate that the use of a realistic distribution functions tends to increase the power flow to the H for the minority heating and to the fast ions for the HHFW heating

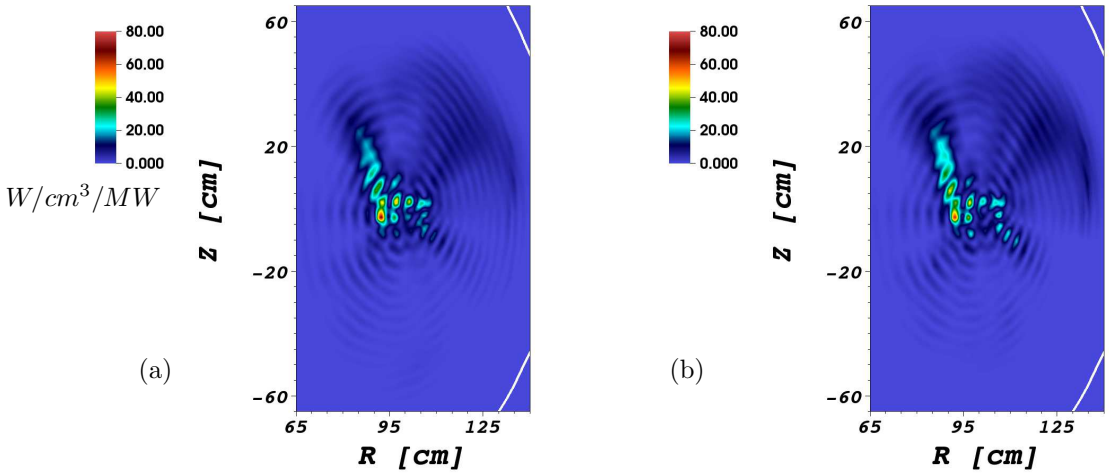

Figure 14. Fast ion absorption profile for:(a) equivalent Maxwellian case; (b) `NUBEAM` non-Maxwellian case

regime.

This work represents a first step towards closing the loop between the extension of `TORIC` in a self-consistent way and the `CQL3D` code for the IC minority heating regime as used, for instance, in Alcator C-MOD experiments and the `NUBEAM` code for HHFW heating regime as used in NSTX-U experiment. This work is done with the aim to be able to make time dependent simulations in TRANSP in a self-consistent way. Work on the quasilinear diffusion coefficients for the finite Larmor radius (FLR) approximation (valid for the IC minority regimes) and on the RF kick-operator in `NUBEAM` are in progress and the results will be presented in a future paper.

Acknowledgments

The authors would like to thank Dr. P. T. Bonoli for the useful discussions. Moreover, the authors thank Dr. R. Bell, Dr. B. LeBlanc, and Dr. S. Sabbagh that have provided the data for the kinetic profiles and magnetic equilibrium. This work was supported by the SciDAC Center for Wave- Plasma Interactions under DE-FC02-01ER54648 and the US DOE under DE-AC02-CH0911466.

References

[1] T. H. Stix. *Nucl. Fusion*, 15:737, 1975.
[2] E. F. Jaeger and et al. *Phys. Plasmas*, 8:1573, 2001.
[3] W. Harvey and M. McCoy. In *Proceedings of the IAEA Technical Committee Meeting on Simulation and Modeling of Thermonuclear Plasmas*, page 489, 1992.
[4] Yu V Petrov and R. W. Harvey. *Plasma Phys. Control. Fusion*, 58:115001, 2016.
[5] E F Jaeger and et al. *Phys. Plasmas*, 13:056101, 2006.
[6] D Smithe. *Plasma Phys. Control. Fusion*, 31:1105, 1989.
[7] R. J. Dumont. *Phys. Plasmas*, 12:042508, 2005.
[8] S. Murakami and et al. *Nucl. Fusion*, 46:S425, 2006.
[9] M Brambilla and R Bilato. *Nucl. Fusion*, 49:085004, 2009.
[10] R Bilato and et al. *Nucl. Fusion*, 51:103034, 2011.
[11] E. Lerche and et al. *Plasma Phys. Control. Fusion*, 51:044006, 2009.
[12] M Choi and et al. *Phys. Plasmas*, 17:056102, 2010.
[13] M Jucker and et al. *Comp. Phys. Comm.*, 182:912, 2011.
[14] R. J. Dumont. *Nucl. Fusion*, 49:075033, 2009.
[15] R. J. Dumont and D. Zarzoso. *Nucl. Fusion*, 53:013002, 2013.
[16] T. Hellsten and et al. *Nucl. Fusion*, 53:093004, 2013.
[17] M Brambilla. *Plasma Phys. Control. Fusion*, 41:1, 1999.
[18] M. Brambilla. *Plasma Phys. Control. Fusion*, 44:2423, 2002.
[19] R. J. Hawryluk. volume 1, page 19, 1980.
[20] P. T. Bonoli and etal. *Phys. Plasmas*, 7:1886, 1999.
[21] S. M. Kaye. *Nucl. Fusion*, 55:104002, 2015.
[22] T. H. Stix. *Waves in Plasmas*. American Institute of Physics, NY, 1992.
[23] C K Phillips and et al. *AIP Conference Proceedings*, 694:499, 2003.
[24] B D. Fried and S D Conte. *Conte. The Plasma Dispersion Function*. Academic Press, NY, 1961.
[25] J C Wright and et al. *Commun. Comput. Phys.*, 4:545, 2008.
[26] R. Bilato and et al. *Adv.Comput. Math.*, 40:1159, 2014.
[27] N. Bertelli and et al. *AIP Conf. Proc.*, 1580:310, 2014.
[28] R. J. Goldston and et al. volume 43. 1981.
[29] A. Pankin and et al. *Comput. Phys. Commun.*, 159:157, 2004.
[30] D. B. Batchelor, E. F. Jaeger, and Colestock P. L. *Phys. Fluids B*, 1:1174, 1989.
[31] J. P. Lee and et al. *Bull Am. Phys. Soc.*, 60:242, 2015.
[32] A. C Bader. *PhD thesis*, 2012.
[33] A. Bader and et al. *Nucl. Fusion*, 52:094019, 2012.
[34] D. L. Green and et al. *Journal of Physics: Conference Series*, 180:012058, 2009.
[35] D. L. Green and et al. *AIP Conf. Proc.*, 1187:569, 2009.
[36] E. D. Fredrickson and etal. *Nucl. Fusion*, 55:013012, 2015.

PPPL PRINCETON PLASMA PHYSICS LABORATORY

Princeton Plasma Physics Laboratory
Office of Reports and Publications

Managed by
Princeton University

under contract with the
U.S. Department of Energy
(DE-AC02-09CH11466)

P.O. Box 451, Princeton, NJ 08543
Phone: 609-243-2245
Fax: 609-243-2751

E-mail: publications@pppl.gov

Website: http://www.pppl.gov